Ocean Engineering 347 (2026) 123917

Contents lists available at ScienceDirect

Ocean Engineering

journal homepage: www.elsevier.com/locate/oceaneng

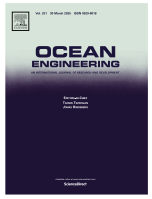

Implementation and validation of boundary element method for corrosion protection

Stefan de Gijsel [a,*], Nick J. Schilder [a], Frits Kernkamp [a], Bart Jan Peet [a], Eugene Lepelaars [a,b]

[a] Netherlands Organisation for Applied Scientific Research, 2509 JG, The Hague, The Netherlands
[b] Delft Institute of Applied Mathematics, Delft University of Technology, 2600 AA, Delft, The Netherlands

ARTICLE INFO

Keywords:
boundary element method
electrostatics
cathodic protection
ICCP
corrosion
physical scale model

ABSTRACT

A boundary element method was developed to estimate electric potential and current density distribution around a ship hull. The model can be used for corrosion diagnosis and the estimation of coating damage. The implementation includes fast analytical integral computations, discontinuous elements, a damped Newton-Raphson method for non-linear boundary conditions due to polarization curves, support for stratified conductivity and an iterative method to simulate impressed current cathodic protection behavior. The model was validated using an analytical benchmark with two cylinders. Furthermore, the model was validated experimentally using a ship scale model, with good results. This model may find useful applications in corrosion diagnosis and coating damage estimation.

1. Introduction

Corrosion protection is an important consideration during ship design. Impressed current cathodic protection (ICCP) systems or sacrificial anodes release current in the electrolyte to make the surface to be protected cathodic. Corrosion and corrosion protection currents additionally result in an underwater electric field. Especially in the design of naval platforms it is important to minimize this electric signature because this signal can be exploited by detection systems (Donati and Le Cadre, 2002).

Numerical computational tools based on the Boundary Element Method (BEM) are often used to analyze cathodic protection designs (Telles et al., 1984; Aoki et al., 1988; Aoki and Kishimoto, 1991; Riemer and Orazem, 2005; Kim et al., 2018; Kalovelonis et al., 2020; Pratt et al., 2022; Nale et al., 2023). Models based on BEM require only meshing of the boundaries of the geometry, resulting in a small number of unknown compared to the Finite Element Method (FEM).

A challenge in the use of BEM formulations is that dense matrices are created because all interactions between elements are included in the system matrices. Both assembly and solution of the resulting linear systems is therefore computationally expensive for large problems. These problems are amplified when non-linear polarization curves are used boundary conditions. These polarization curves describe the relationship between surface currents and surface potential. The iterative schemes that are used to solve these non-linear problems result in a large number of linear systems that have to be solved for a single configuration. Furthermore, in the design phase of a ship it is hard to predict where coating damages will occur. It is therefore good practice to simulate a large number of scenarios where damages are placed on different parts of the hull. BEM codes are also used in inverse analysis (Wrobel and Miltiadou, 2004; Guibert et al., 2009; Chung et al., 2011). When readings of the reference electrode potentials are coupled to an inverse model, information can be retrieved about the distribution of currents and potentials over the ship hull and consequently about the state of the coating. A computationally efficient BEM formulation is required for solving these inverse problems.

Rigorous experimental verification of BEM models for corrosion protection design is an equally challenging task. Polarization curves of materials have a large influence on simulations and experimental results (Kim et al., 2018). The behavior of materials can vary significantly over time, between different material samples and with varying environmental conditions. It is therefore difficult to obtain these curves with sufficient accuracy. This makes it difficult to distinguish numerical inaccuracies from experimental variability. The uncertainty in polarization behaviour limits confidence in the predictive accuracy of the use of BEM codes for cathodic protection design.

This work introduces a computationally efficient and robust BEM implementation for corrosion protection and electric signature prediction. The main contribution of this work is the twofold validation of a BEM code that demonstrates its predictive abilities. First of all the

* Corresponding author.
E-mail addresses: stefan.degijsel@tno.nl (S. de Gijsel), nick.j.schilder@gmail.com (N.J. Schilder), frits.kernkamp@tno.nl (F. Kernkamp), bart_jan.peet@tno.nl (B.J. Peet), eugene.lepelaars@tno.nl (E. Lepelaars).

https://doi.org/10.1016/j.oceaneng.2025.123917
Received 12 September 2025; Received in revised form 22 November 2025; Accepted 4 December 2025
Available online 20 December 2025

correct numerical results are compared with an analytical benchmark problem. Secondly, numerical solutions are compared to experimental data acquired with a physical scale-model (PSM) setup that was developed specifically for this purpose. The setup allows for detailed measurement of the electric field distribution below the PSM, providing a level of experimental resolution not previously reported in literature.

Physical scale models (PSM) have been used in the past for the validation of BEM codes (Hack and Janeczko, 1993; DeGiorgi et al., 1998; Wang and KarisAllen, 2010). By scaling down the conductivity of the electrolyte with the dimension of the real ship, the potential differences between surface elements can be kept the same with respect to the full size ship (Ditchfield et al., 1995). The PSM described in this work is modular, which means that different configurations of propellers, impressed current and sacrificial anodes, reference cells and steel patches can be added. The BEM code and PSM measurements are compared using a two-dimensional sensor array which measures the electric fields underneath the PSM. Compared to earlier published work about PSM experiments (Guibert et al., 2010; Ding-feng et al., 2016; Huan et al., 2023) the facility is able to provide more detailed insight in the distribution of electric fields below the PSM, resulting in a more detailed comparison between model and measurements.

The BEM implementation in this work is efficient in several ways. First, the code makes use of linear elements for the interpolation of the unknown potentials and normal derivatives of the potentials. The advantage of the use of linear elements over constant elements is that the potential varies linearly over a single element. This reduces the number of elements required for the same computational accuracy, especially at locations where large potential gradients are expected to occur. Secondly, the integrals evaluated over the boundary elements that occur in the system matrix are solved analytically. The boundary integrals can therefore be evaluated faster than with high order numerical integration. The solutions of the integrals are also exact and therefore provide higher precision than numerical evaluation with quadrature rules. Other solutions to improve the speed of assembly and solution of BEM systems also exist. The fast multipole method (FMM) (Greengard and Rokhlin, 1997; Keddie et al., 2007) or a combination of hierarchical matrices and adaptive cross approximation (ACA) (Ostrowski et al., 2006; Smajic et al., 2007) result in efficient use of memory and smaller assembly and solutions times. The code presented in this paper could be extended with this type of functionality to make it even faster.

Several other features were added to the BEM to increase its robustness. In a BEM it is assumed that the geometry is continuous. Due to badly defined normal vectors at sharp corners, or undefined node materials at the interface between different materials, numerical problems can occur. Discontinuous elements were introduced to mitigate these problems. By placing evaluation points slightly away from the mesh nodes numerical problems are circumvented. Other BEM implementations in the literature cope with these challenges at the level of the integral formulation (Andjelić et al., 2007; Smajic et al., 2006). Secondly, simulations with non-linear polarization curves are solved by making use of the Newton-Raphson method. In some cases this iterative scheme does not converge, especially when non-smooth experimental data is used as a boundary condition. The introduction of a relaxation parameter in the code ensures that the method converges in those cases (Sun, 2002). The simulation of the control of the ICCP system by incorporating potential readings on reference cells is integrated in the iterative scheme. Finally, environmental influences on the behavior of the corrosion protection systems and the electric signature can also be taken into account in the code. With the use of the method of images multiple layers with different conductivities can be included in the simulations.

In Section 2 of this paper the BEM code is explained in detail. This includes (a) a method to incorporate layers with varying conductivity, (b) analytic solutions for integrals over linear elements, (c) the treatment of discontinuities at the boundary, (d) an iterative procedure to include polarization curves in the solution, (e) a method to include randomized damage distributions in the simulations and (f) the simulation of ICCP system control. In Section 3 a benchmark problem is presented for which an analytical solution exists. The analytical solution is then compared to the numerical solution of the BEM code. In Section 4 the PSM facility is discussed. The experiments are described and the resulting data is compared to simulations with the BEM code.

2. BEM

2.1. Standard BEM model

The boundary element method (BEM) is an established method for solving electric potential problems. The method is set up starting from the Laplace equation for the electric potential ϕ, for a point $\mathbf{r}$ in some volume V:

$$\nabla^2\phi(\mathbf{r}) = 0. \tag{1}$$

For the 3D Laplace operator, Green's function for a source located at position $\mathbf{r}_0$ is

$$G(\mathbf{r};\mathbf{r}_0) = -\frac{1}{4\pi|\mathbf{r}-\mathbf{r}_0|}. \tag{2}$$

After applying the divergence theorem an integral equation over the boundary ∂V of the volume appears:

$$-c(\mathbf{r}_0)\phi(\mathbf{r}_0) = \oiint_{\partial V}\left[\phi(\mathbf{r})\frac{\partial G(\mathbf{r};\mathbf{r}_0)}{\partial n} - G(\mathbf{r};\mathbf{r}_0)\frac{\partial\phi(\mathbf{r})}{\partial n}\right]\mathrm{d}^2r, \tag{3}$$

where c is a coefficient between 0 and 1, equal to $\frac{1}{2}$ for $\mathbf{r}_0$ at a smooth boundary and equal to 1 for $\mathbf{r}_0$ inside the volume V.

Consider now an infinite electrolyte volume, and suppose it has a boundary of finite size ∂V_c, and some boundary infinitely far away from ∂V_C. Then one can replace the integral over the latter by an electric potential at infinity ϕ_∞:

$$\begin{aligned} c(\mathbf{r}_0)\phi(\mathbf{r}_0) &= \phi_\infty \\ &+ \oiint_{\partial V_C}\left[-\phi(\mathbf{r})\frac{\partial G(\mathbf{r};\mathbf{r}_0)}{\partial n} + G(\mathbf{r};\mathbf{r}_0)\frac{\partial\phi(\mathbf{r})}{\partial n}\right]\mathrm{d}^2r. \end{aligned} \tag{4}$$

To solve the corrosion protection problem, the boundary of the geometry is meshed using triangular elements. For each node i a basis function $b_i(\mathbf{r})$ is introduced which is 1 in $\mathbf{r}_i$, 0 in all other nodes and linear on the triangular elements surrounding $\mathbf{r}_0$. Consider a linear triangular element A with vertices $\mathbf{r}_1$, $\mathbf{r}_2$, and $\mathbf{r}_3$, and outward pointing normal vectors of the edges - $\mathbf{n}_1$ for the edge between $\mathbf{r}_2$ and $\mathbf{r}_3$, $\mathbf{n}_2$ for the edge between $\mathbf{r}_3$ and $\mathbf{r}_1$, and $\mathbf{n}_3$ for the edge between $\mathbf{r}_1$ and $\mathbf{r}_2$. The basis function associated with node 1 has the following values on A:

$$b_1(\mathbf{r}) = \frac{(\mathbf{r}-\mathbf{r}_2)\cdot\mathbf{n}_1}{(\mathbf{r}_1-\mathbf{r}_2)\cdot\mathbf{n}_1}. \tag{5}$$

The equation for a node k becomes:

$$\begin{aligned} c_k\phi_k =& \phi_\infty + \sum_{i=1}^{N}\left[\phi_i\iint_{A_i} b_i(\mathbf{r})\frac{\partial G(\mathbf{r};\mathbf{r}_k)}{\partial n}\mathrm{d}^2r\right. \\ &\left. - \left[\frac{\partial\phi}{\partial n}\right]_i\iint_{A_i} b_i(\mathbf{r})G(\mathbf{r};\mathbf{r}_k)\mathrm{d}^2r\right], \end{aligned} \tag{6}$$

where A_i denotes the surfaces of all triangular elements surrounding node i.

For each node, one of the following is known: the electric potential, the normal derivative of the electric potential (for example for insulators), or a local relation between electric potential and its normal derivative - described by a polarization curve. After evaluating the integrals, which is described in Section A, (6) results in a linear system of equations if all polarization curves are linear:

$$A\mathbf{x} = B\mathbf{b}, \tag{7}$$

where all unknown values are moved to vector $\mathbf{x}$, and all known values to vector $\mathbf{b}$.

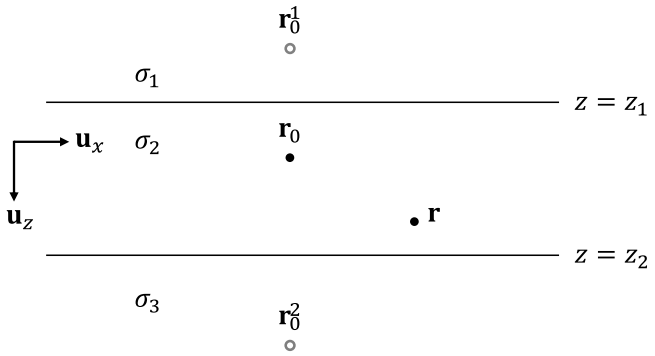

Fig. 1. Schematic of the three layer medium, including the first two reflections of $\mathbf{r}_0$ in gray.

2.2. Electrolyte interfaces and stratified conductivity

The BEM can be adapted for the case where different layers of conductivity are present, for example at an interface between air and water, or in the case of stratified conductivity (Peratta et al., 2017). This is done using mirrored sources with a magnitude dependent on the conductivity of the different layers. Up to three layers can be used. For each interface a transmission and reflection coefficient is calculated based on the conductivity values σ_1 of layer 1 and σ_2 of layer 2:

$$T_{21} = \frac{2\sigma_2}{\sigma_1 + \sigma_2}, \tag{8}$$

$$R_{21} = \frac{\sigma_1 - \sigma_2}{\sigma_1 + \sigma_2}. \tag{9}$$

In an environment with one interface at $z = 0$, where σ_1 is the conductivity for $z < 0$ and σ_2 is the conductivity for $z > 0$, the Green's functions are given by:

$$G(\mathbf{r};\mathbf{r}_0) = \frac{1}{4\pi}\frac{T_{21}}{|\mathbf{r}-\mathbf{r}_0|}, \quad z < 0, \tag{10}$$

$$G(\mathbf{r};\mathbf{r}_0) = \frac{1}{4\pi}\left(\frac{1}{|\mathbf{r}-\mathbf{r}_0|} - \frac{R_{21}}{|\mathbf{r}-\mathbf{r}_0^3|}\right), \quad z > 0, \tag{11}$$

where $\mathbf{r}_0^3$ is the position of $\mathbf{r}_0$ mirrored at the interface.

Repeated mirroring can describe a three-layer environment consisting of (1) air, (2) seawater and (3) seabed with corresponding reflection coefficients R_{21} and R_{23} at the two interfaces. For this environment, the Green's function in the middle layer (layer 2) is given by

$$G(\mathbf{r};\mathbf{r}_0) = -\frac{1}{4\pi}\left[\sum_{n=0}^{\infty}\frac{(R_{21}R_{23})^n}{|\mathbf{r}-\mathbf{r}_0^{(12)^n}|} + \sum_{n=1}^{\infty}\frac{(R_{21}R_{23})^n}{|\mathbf{r}-\mathbf{r}_0^{(21)^n}|} - R_{23}\sum_{n=0}^{\infty}\frac{(R_{21}R_{23})^n}{|\mathbf{r}-\mathbf{r}_0^{2(12)^n}|} - R_{21}\sum_{n=0}^{\infty}\frac{(R_{21}R_{23})^n}{|\mathbf{r}-\mathbf{r}_0^{1(12)^n}|}\right], \tag{12}$$

where the mirrored source positions for a point $\mathbf{r}_0 = (x_0, y_0, z_0)$ are given by

$$\mathbf{r}_0^{(12)^n} = x_0\mathbf{u}_x + y_0\mathbf{u}_y + [2n(z_2 - z_1) + z_0]\mathbf{u}_z, \tag{13}$$

$$\mathbf{r}_0^{(21)^n} = x_0\mathbf{u}_x + y_0\mathbf{u}_y + [-2n(z_2 - z_1) + z_0]\mathbf{u}_z, \tag{14}$$

$$\mathbf{r}_0^{2(12)^n} = x_0\mathbf{u}_x + y_0\mathbf{u}_y + [2z_2 + 2n(z_2 - z_1) - z_0]\mathbf{u}_z, \tag{15}$$

$$\mathbf{r}_0^{1(12)^n} = x_0\mathbf{u}_x + y_0\mathbf{u}_y + [2z_1 - 2n(z_2 - z_1) - z_0]\mathbf{u}_z, \tag{16}$$

with $\mathbf{u}_x, \mathbf{u}_y, \mathbf{u}_z$ being the unit vectors in each direction. An illustration of this situation is shown in Fig. 1.

An infinite number of reflected sources is required for an exact solution. In practice, one needs to cut off the summation after $n_{\max}$ terms.

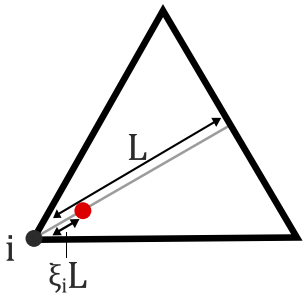

Fig. 2. Illustration of the placement of an evaluation node in case discontinuous elements are applied.

2.3. Discontinuous elements

In the basic version of the BEM with linear elements as described above, the electric potential and its normal derivative are assumed continuous over the boundary. This gives problems in two situations:

noitemsep The elements around a node form a sharp corner.
noiitemsep The node lies on a material boundary.

In case 1, it is unclear what normal vector should be assigned to the node in question - the normal vectors of the surrounding elements are well-defined, but that of the node is not. In case 2, the material and therefore boundary condition of a node on the edge between two different materials is not defined.

To solve these problems, it suffices to locally drop the assumption that the electric potential and its normal derivative must be continuous. This can be done by introducing discontinuous elements (Kythe, 1995; Patterson and Sheikh, 1981; Wang et al., 2022). Evaluation node i is shifted inside the mesh triangles, along the internal bisector with ξ_i times the length of that bisector, away from the geometrical node at the corner. Usually the factor ξ_i is small, in the order of 0.01. This is illustrated in Fig. 2. At such a new evaluation node, the material and normal vector are well-defined - namely that of the triangular element the evaluation node lies in.

The values of the integrals in (6) in the newly defined evaluation nodes are a linear combination of the previously evaluated integral values of the geometrical nodes. This is described by the transformation matrix

$$Q = \begin{pmatrix} 1-\xi_1 & \xi_1/2 & \xi_1/2 \\ \xi_2/2 & 1-\xi_2 & \xi_2/2 \\ \xi_3/2 & \xi_3/2 & 1-\xi_3 \end{pmatrix}^{-1}. \tag{17}$$

The potentials at the corners, ϕ_i, are related to the potentials at the evaluation nodes, ϕ_i', by

$$\begin{pmatrix}\phi_1 \\ \phi_2 \\ \phi_3\end{pmatrix} = Q\begin{pmatrix}\phi_1' \\ \phi_2' \\ \phi_3'\end{pmatrix}. \tag{18}$$

As an example consider the integral over one of the triangular surfaces A (other integrals are evaluated in a similar manner):

$$u_i = \iint_A b_i(\mathbf{r})\frac{\partial G(\mathbf{r};\mathbf{r}_0)}{\partial n}\mathrm{d}^2 r. \tag{19}$$

Then the full integral over a discontinuous element is given by

$$\sum_{i=1}^{3}\phi_i u_i = \sum_{j=1}^{3}\phi_j' u_j', \tag{20}$$

where the new integral values at the evaluation points are given by

$$u_j' = \sum_{i=1}^{3} Q_{i,j}u_i. \tag{21}$$

2.4. Polarization curves

A polarization curve valid for evaluation node m can be defined as a function

$$\phi_i = f_i\left(\frac{\partial\phi}{\partial n}\right), \tag{22}$$

where

$$-\sigma\frac{\partial\phi}{\partial n} = \mathbf{J}\cdot\mathbf{n}, \tag{23}$$

with $\mathbf{J}$ the current density and $\mathbf{n}$ the normal vector.

Inserting this relation in (6) results in an unknown term $f_i\left(\frac{\partial\phi}{\partial n}\right)$ which makes the resulting system non-linear:

$$\mathbf{h}(\mathbf{x}) = A\mathbf{x} - B\mathbf{b}(\mathbf{x}) = \mathbf{0}. \tag{24}$$

An iterative scheme is needed to solve the new system. As a numerical solver, a damped version of the multivariate Newton-Raphson method was used (Sun, 2002). The iteration step is given by

$$\mathbf{x}_{n+1} = \mathbf{x}_n - J_h(\mathbf{x}_n)^{-1}\mathbf{h}(\mathbf{x}_n). \tag{25}$$

Here the Jacobian is given by

$$J_h(\mathbf{x}_n) = A - \alpha B\nabla\mathbf{b}(\mathbf{x}_n), \tag{26}$$

where α is the damping factor, which is chosen from the interval $(0, 1)$, and A and B are as in (7). The damping factor is decreased over various tries until the method converges. For the problem in this paper, a damping factor of 0.1 was used, yielding convergence within 10 iterations.

2.4.1. Damage

In order to describe damage of a coated ship hull, the term *damage fraction* d_n is introduced as a number between 0 and 1 which represents the local damage at node $\mathbf{r}_n$. A value of 0 means that the coating is intact and perfectly electric insulating, whereas a value of 1 means that the coating has completely disappeared and uncoated metal is in direct contact with the electrolyte. The method of simulating damage present on a ship hull consists of

noitemsep giving all nodes a damage fraction between 0 and 1;
noiitemsep scaling the local polarization curve.

The vector of damage fractions for all evaluation nodes d is drawn from the distribution

$$\mu + L\mathcal{N}(0, 1). \tag{27}$$

Here $\mathcal{N}(0, 1)$ is the standard normal distribution, μ is the average damage fraction, and L is created from a Cholesky decomposition

$$K + 10^{-6}I = LL^T, \tag{28}$$

where K is a Gaussian kernel with correlation length l. Its elements are given by

$$K_{i,j} = \exp\left(-\frac{|\mathbf{r}_i - \mathbf{r}_j|^2}{2l^2}\right). \tag{29}$$

Note that the factor of 10^{-6} in (28) is used to ensure that $K + 10^{-6}I$ is positive definite and therefore the decomposition is possible.

An example of a generated random damage distribution applied to the physical scale model geometry, which will be described in more detail in Section 4, is shown in Fig. 3.

For each evaluation node i, the polarization curve is scaled by a damage fraction d_i according to

$$\phi_i = f_i\left(\frac{1}{d_i}\frac{\partial\phi}{\partial n}\right). \tag{30}$$

Indeed, if $d_i = 1$ the original polarization curve f_i is used, and in the limit $d_i \to 0$ the adjusted polarization curve approaches the line $\frac{\partial\phi}{\partial n} = 0$ corresponding to a perfect insulator.

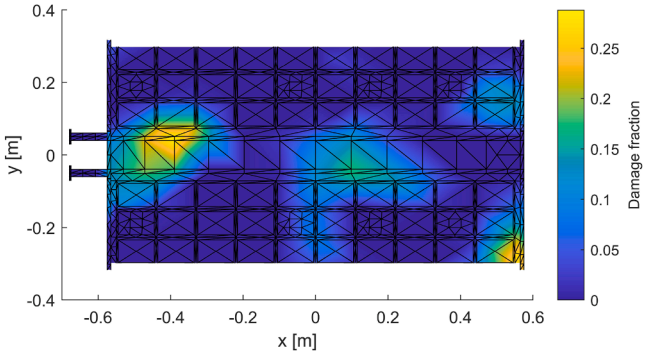

Fig. 3. Random damage distribution applied to the physical scale model geometry, with parameters $\mu = 0.0065$ and $l = 0.12$ m.

2.5. ICCP simulation

An ICCP system with a number of impressed current anodes is supported in the BEM implementation using different options:

noitemsep The total applied current is fixed for each of the anodes.
noiitemsep The electric potential at a reference cell - a node on the boundary - is fixed.
noiiitemsep The electric potential at a reference cell lies between two fixed values.

For option 1, it is assumed that the electric potential over each impressed current anode surface is constant but unknown. For an impressed current anode containing n evaluation nodes, this gives n equations and one unknown. Each electric potential normal derivative is considered unknown, yielding a total of $n + 1$ unknowns. The total applied current is set as a boundary condition, bringing the total to $n + 1$ equations. Hence, the linear system has a unique solution.

In option 2, an electric target potential at a reference cell located on the boundary is given per impressed current anode. Just as for option 1, the electric potential is assumed constant but unknown, and its normal derivative is unknown at every evaluation node. If the reference cell is located exactly at a boundary node, then the final equation of the linear system is given by setting the node's electric potential to the target reference electric potential as a boundary condition. If the reference cell is located between boundary nodes, then a weighted mean between the evaluation nodes surrounding the reference cell location is set equal to the target electric potential.

With option 3, the true behavior of an ICCP system is simulated. Beforehand, for each reference cell i a desired electric potential range $[\phi_{i,\min}, \phi_{i,\max}]$ is defined. In an iterative method, the anode currents are varied. For each iteration, a system is solved according to option 1. A new set of anode currents is determined based on the previous current step and the observed difference in electric potential at the corresponding reference cell. For a reference cell and anode pair i, the anode current I in iteration $k + 1$ is updated according to

$$I_{k+1} = \frac{I_k - I_{k-1}}{\phi_k - \phi_{k-1}}(\phi_i^* - \phi_k), \tag{31}$$

where ϕ_k is the observed electric potential at the reference cell, and ϕ_i^* is the desired reference potential (the mean of $\phi_{i,\min}$ and $\phi_{i,\max}$). The iterative procedure is executed until all reference potentials are within the specified range. Note that the underlying assumption of this option is that each impressed current anode only influences the reference potential measured on its corresponding reference cell, and not the other reference potentials. In practice, this may not be the case, and if impressed current anodes heavily influence other reference cells, the desired reference potentials may not be reached. In that case, the procedure is stopped after a specified maximum number of iterations.

3. Analytical validation

3.1. Problem description

The BEM code was applied to calculate the electrostatic potential for two equipotential infinite cylinders emerged in water. The solution was compared to its analytical solution. As the BEM algorithm works only for finite geometries, the solution needs to be approximated. To this end, a situation is considered with two finite cylinders in water, sandwiched between two semi-infinite layers of electrical insulators ($\sigma = 0$ S/m). The solution of this problem in the limit of infinite reflections is equal to the solution of two infinitely extended cylinders. Fig. 4(a) shows the configuration under study, where $L = 5$ m, $R_1 = R_2 = 1$ m and $-x_1 = x_2 = 2$ m. The electric potentials applied to the left and right cylinder are $\phi_1 = -1$ V and $\phi_2 = -0.25$ V, respectively.

3.2. Analytical solution

The problem of two infinite cylinders can be considered a 2D problem, where two circles with potentially different radii are considered. Key to finding the analytical solution of the Laplace equation with Dirichlet boundary conditions is to find a coordinate system for which the circles are isocurves. The solution of the Laplace equation for two isocurves at a fixed potential is typically easier to solve. It turns out that bipolar coordinates are appropriate and the Laplace equation is invariant under the coordinate transformation from Cartesian coordinates to bipolar coordinates (ι, σ). A circle with radius R_i and center $(x_c, y_c) = (x_i, 0)$ in a Cartesian reference frame is given by a line through

$$\tau_i = \text{sign}(x_i)\text{acosh}\left(\left|\frac{x_i}{R_i}\right|\right). \tag{32}$$

When considering both circles placed along $y = 0$, and placed on opposite side of $y = 0$, so that $\tau_1 < 0$ and $\tau_2 > 0$, the solution to the Laplace equation is of the form:

$$\phi(\tau) = c_1\tau + \phi_\infty. \tag{33}$$

Since infinitely far away from the circles corresponds to $\tau = 0$, the last constant is already set equal to the potential at infinity. Solving for the two potentials results in

$$\phi(\tau) = \frac{\phi_2 - \phi_1}{|\tau_1| + |\tau_2|}\tau + \frac{|\tau_2|\phi_1 + |\tau_1|\phi_2}{|\tau_1| + |\tau_2|}. \tag{34}$$

It is interesting to observe that indeed the potential at infinity is given by a weighted average of the two different potentials. Transforming back to Cartesian coordinates results into:

$$\phi(x, y) = \frac{1}{\text{acosh}\left(\left|\frac{x_1}{R_1}\right|\right) + \text{acosh}\left(\left|\frac{x_2}{R_2}\right|\right)}. \tag{35}$$

The analytical solution to this problem is shown in Fig. 4(b).

3.3. Comparison of BEM and analytical solution

Fig. 4(d) shows the solution found by the BEM algorithm when considering only a single reflection of each interface. Comparing Fig. 4(b) and (d) shows that the solution deviates strongest on the edges of this figure. This means in practice that the deviation of the solution grows with the distance to the source. This can intuitively be understood by the fact that the distance from the image sources to the detection point becomes more and more comparable to the distance from the source straight to the detection point, and can therefore not be neglected. Fig. 4(c) shows how the solution at the point $(x, y) =$ (-6 m, 0 m) converges to the analytical solution after considering a few reflections. Note that the computation time of constructing the interaction matrices increases linearly with increasing reflections, since every extra reflection introduces four new source points. The computation time of solving the BEM system does not change with increasing reflections.

To investigate mesh convergence, similar simulations were done with 50 reflections, for five different triangular meshes, with different number of triangular mesh elements. The result in Fig. 5 shows a quadratic convergence of the potential solution for increasing number of elements. For the mesh with most elements (2672), the difference between the analytical solution and the BEM result along a line is shown in Fig. 6.

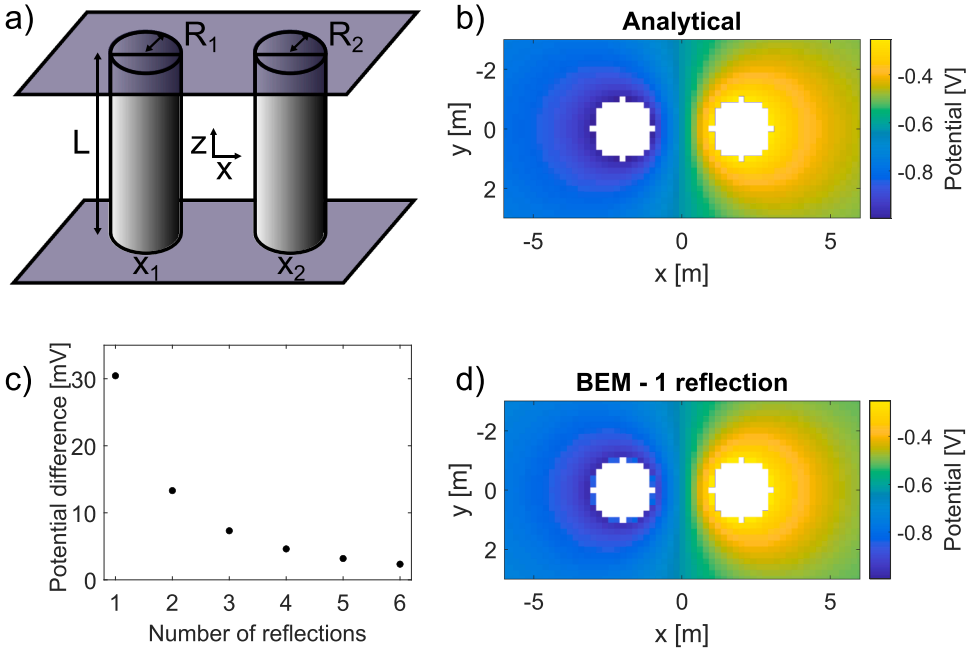

Fig. 4. Benchmark of BEM on analytical model. (a) Configuration to solve with BEM, including the two infinitely extended insulators. (b) Analytical solution of the electrostatic potential in the (x, y)-plane. Black circles illustrate the boundaries of the cylinders. (b,d) Points where no solution has been calculated are left in black. (c) Convergence plot, with the absolute potential difference between the BEM calculated solution and the analytical solution at the point $(x, y) =$ (-6, 0) m. (d) Numerically obtained solution of the electrostatic potential in the plane $z = 0$ m, where only one reflection is considered.

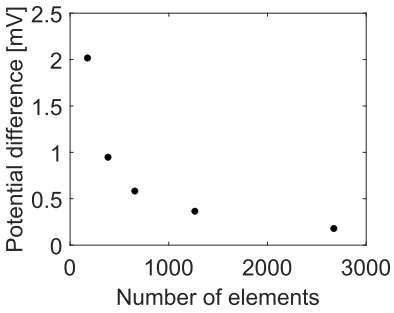

Fig. 5. Mesh convergence for 50 reflections, with the absolute potential difference between the BEM calculated solution and the analytical solution at the point $(x, y) = (-6, 0)$ m.

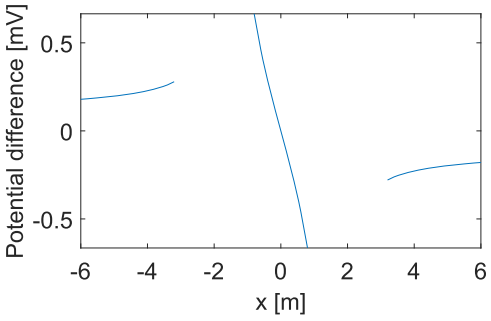

Fig. 6. Difference between the BEM calculated solution and the analytical solution along the line $y = 0$ m, for the mesh with 2672 elements and 50 reflections.

4. Experimental validation

4.1. Experimental setup

A modular electric Physical Scale Model (PSM) of a ship was built using high density polyethylene and was equipped with bronze propellers (nickel-aluminum-bronze, each with an area of 29.5 cm^2), titanium impressed current anodes (Ti, each with an area of 10 cm^2), bare steel patches (S355, each with an area of 90 cm^2) and Ag/AgCl reference cells for 1) controlling the ICCP system and 2) measuring the hull potential, see Fig. 8. The length and width at the top are 1.14 m by 0.64 m, respectively. The lowest point of the PSM is approximately 0.24 m below the water line. The steel patches are located against the waterline, at 4 cm and at 48 cm from the front.

The PSM was placed in a cylindrical basin with a diameter of 6 m, water height of 0.75 m, salinity of 500 µS/cm and water temperature of 20.5 °C. The PSM is centered above an array of 5 x 3 sensor tiles, each 500 mm by 500 mm and consisting of 3 x 3 Ag/AgCl disk electrodes, see Fig. 7. The sensor array measurements are acquired using an Agilent 34980A.

A custom ICCP system for the PSM was designed and constructed by CORROSION. After 72 hours of relaxation with the ICCP system active, the potential distribution below the scale model was measured by the sensor array and current values passing through the NAB, Ti and S355 were acquired using an Agilent 34970A.

The noise on potential measurements of the array sensors is characterized by computing an amplitude spectral density (ASD) from the time signals using the Welch technique. The result is shown in Fig. 9. The majority of sensors shows similar noise characteristics. The noise floor of most sensors lies around 0.01 mV near 0.01 Hz. Furthermore, a noise peak is present around $7 \cdot 10^{-4}$ Hz, corresponding to approximately once every 24 minutes. Possibly, this noise is due to a generator located 3 meters away from the side of the basin.

From the ASD of each array sensor, a root mean square (RMS) noise value can be estimated. This is done by integrating the area below the squared ASD over a frequency band. The RMS noise between 0.001 and 0.01 Hz is calculated and shown in Fig. 10. Most sensors have a RMS noise in the order of 1 µV or less, and about 10 sensors have a larger RMS noise in the order of 10 µV.

Table 1
Measured current values.

Anode aft portside	0.5 mA
Anode aft starboard	0.8 mA
Anode forward portside	2.6 mA
Anode forward starboard	0.8 mA
Propeller portside	1.1 mA
Propeller starboard	1.1 mA
Steel portside	1.3 mA
Steel starboard	1.2 mA

4.2. Experimental results

Sensor array measured data and model prediction of these measurements are compared using two sets of boundary conditions for the propellers, impressed current anodes and steel patches. The first set is formed by imposing current measurements from the steel, NAB and titanium as uniform boundary conditions onto the corresponding regions in Fig. 11. Hence for all nodes i in these regions, $\left[\frac{\partial \phi}{\partial n}\right]_i$ is imposed by dividing the known current uniformly over the material nodes, and then dividing by the conductivity to obtain the potential normal derivative. The currents are provided in Table 4.2.

The second set is formed by imposing measured polarization curves on the steel and NAB regions in Fig. 11. This set is discussed later in this section. The boundary conditions are imposed using (7).

The electric field in the x- and y-directions is calculated from the sensor array potential using a forward difference method. At a reference sensor at location index (m, n), the electric field components are calculated as

$$E_x = \frac{\phi_{m+1,n} - \phi_{m,n}}{\Delta x}; \tag{36}$$

$$E_y = \frac{\phi_{m,n+1} - \phi_{m,n}}{\Delta y}, \tag{37}$$

where $\phi_{m,n}$ is the measured reference potential at location index (m, n), and Δx and Δy are the distances between two neighboring sensors in the respective directions. The total horizontal field $|E|$ is calculated as

$$|E| = \sqrt{E_x^2 + E_y^2}. \tag{38}$$

The sensor array measured electric field, corresponding forward model result and their difference are shown in Fig. 12. Furthermore, a comparison of the electric field on the line $y = 0$ m is shown in Fig. 13.

A relative root mean square (rRMS) difference is computed, defined by

$$\text{rRMS} = \frac{\sqrt{\frac{1}{k}\sum_{i=1}^{k} |E_{\text{measured}} - E_{\text{estimate}}|^2}}{\max\left(|E_{\text{measured}}|\right)}, \tag{39}$$

where i loops over the $k = 112$ electric field values below the scale model. The resulting value for rRMS is 6.4%.

Polarization curves for S355 and NAB were measured using a PalmSens4 potentiostat and are shown in Fig. 14. These are used as an alternative set of boundary conditions in the BEM to allow a second comparison of the simulated electric field to the measured electric field, see Fig. 15 and Fig. 16. The resulting value for rRMS is now 7.6%. A possible reason for lower performance is a changed corrosion state of the materials due to air exposure. Furthermore, no compensation for the ohmic drop between reference electrode and material was applied, which may lead to an error in the polarization curves.

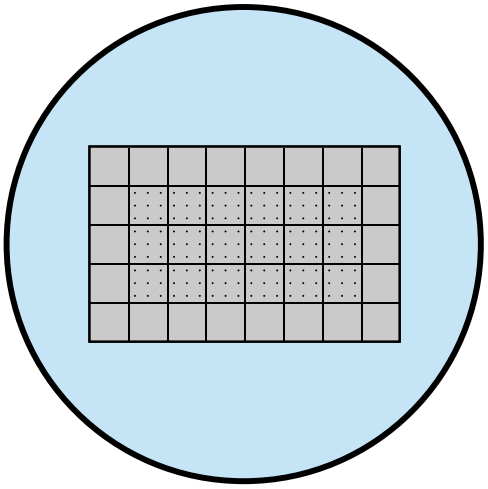

Fig. 7. Top view of the basin with sensor array. The array is surrounded by extra tiles without reference cells. The scale model is centered above the sensor array during measurements.

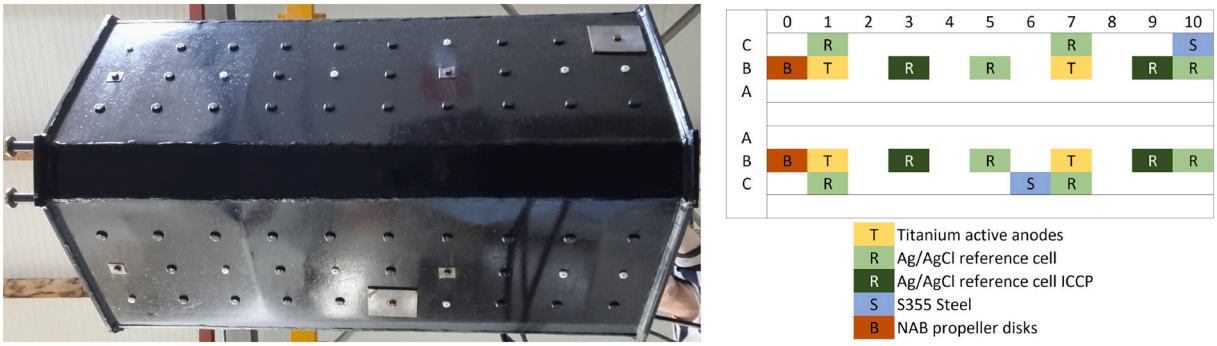

Fig. 8. Modular physical scale model (PSM) of a ship, along with a schematic representation of the PSM. Note that the picture is mirrored in the vertical direction, to compare to the schematic.

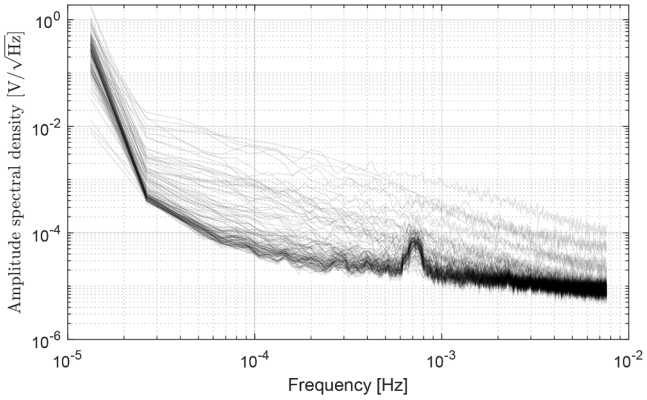

Fig. 9. Amplitude spectral density (ASD) plot of all array sensors.

To investigate which portion of the rRMS difference can be attributed to noise in the potential measurements, the following procedure is followed: for each sensor a noise value is drawn from a normal distribution with zero mean and the respective RMS noise value from Fig. 10 as standard deviation. The electric field corresponding to this noise realization is calculated and the rRMS difference is calculated as before. This procedure is repeated 10,000 times and the results are summarized in a histogram of the rRMS noise in Fig. 17. This histogram indicates that rRMS difference values of up to 0.5% can be attributed to noise in potential measurements.

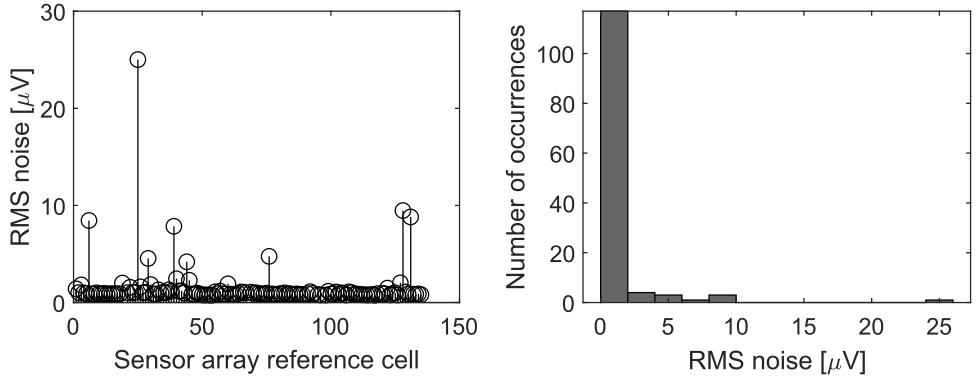

Fig. 10. Noise RMS values, computed for the frequency band between 0.001 and 0.01 Hz, per array sensor, and a histogram of these values.

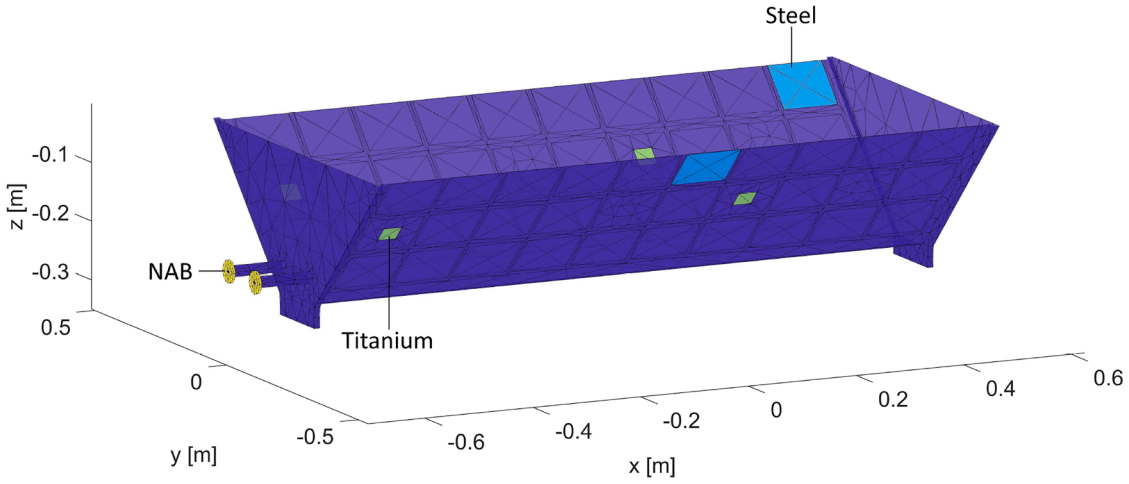

Fig. 11. Scale model regions to which different boundary conditions are applied.

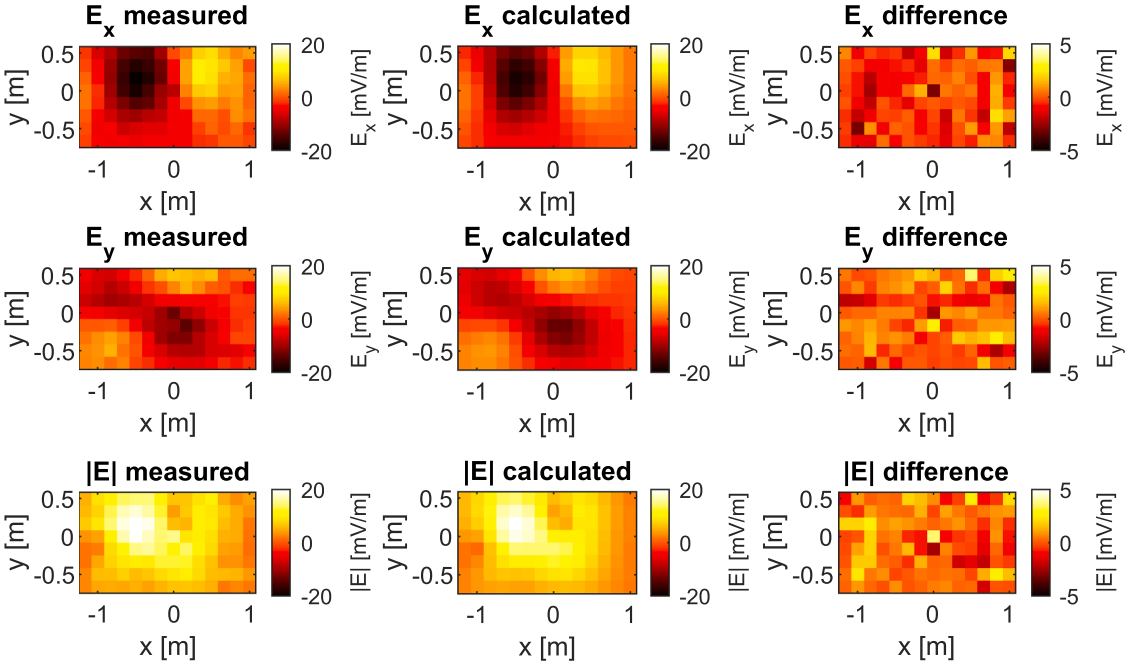

Fig. 12. Left) electric field from sensor array measurement. Middle) measured current values per surface area are used as boundary conditions for a forward computation of the electric field at the sensor array. Right) difference between the measured and simulated electric field values.

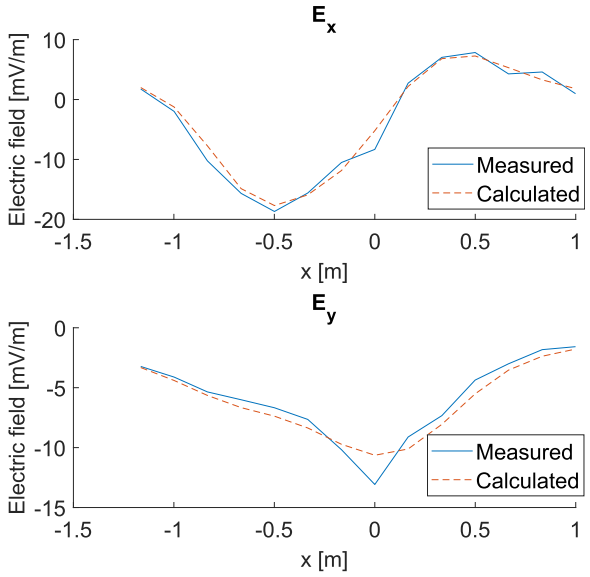

Fig. 13. Electric field from sensor array measurement and resulting from a BEM computation using measured current values per surface area as boundary conditions, on the line $y = 0$ m.

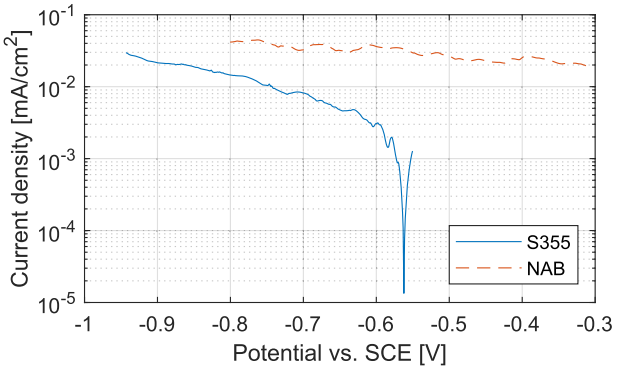

Fig. 14. PalmSens4 measured polarization curves. Potential is given versus saturated calomel electrode (SCE) potential.

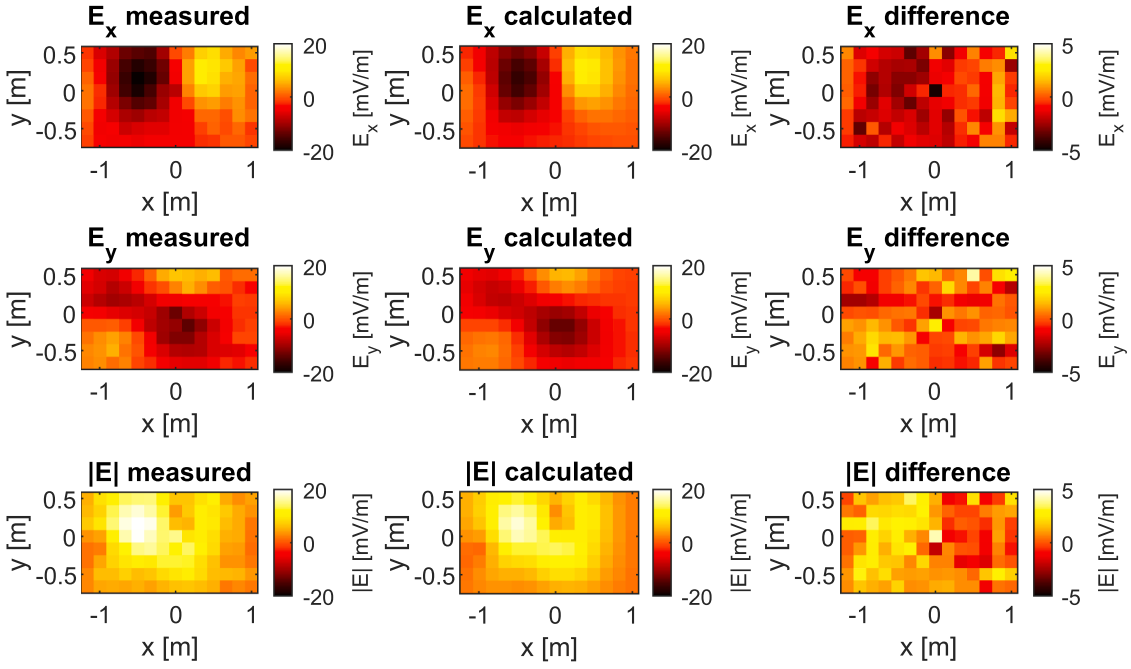

Fig. 15. Left) electric field from sensor array measurement. Middle) in situ measured polarization curves are used as boundary conditions for a forward computation of the electric field at the sensor array. Right) difference between the measured and simulated electric field values.

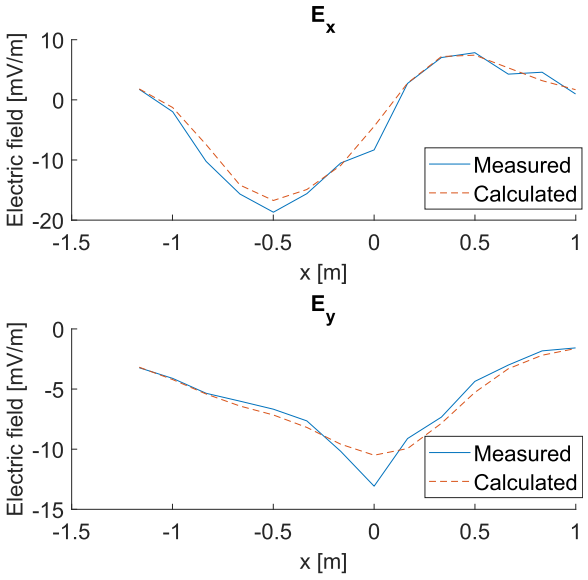

Fig. 16. Electric field from sensor array measurement and resulting from a BEM computation using in situ measured polarization curves as boundary conditions, on the line $y = 0$ m.

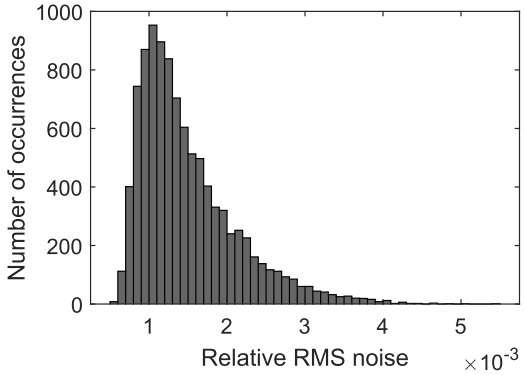

Fig. 17. Expected relative RMS difference due to measurement noise in sensor array.

5. Conclusion

The BEM is an efficient method for solving (semi-)infinite electric potential problems. A BEM was developed to estimate electric potential and current density distribution around a ship hull. The model can be used for corrosion diagnosis and the estimation of coating damage.

Functionality to model stratified conductivity and electrolyte interfaces has been implemented through a truncated set of mirrored sources. Analytical solutions have been determined for linear elements. A local discontinuous elements functionality was implemented to solve problems in regions with sharp corners and material boundaries. To simulate polarizing materials a polarization curve functionality has been implemented with the capability to generate coating damage distributions.

Furthermore, three different procedures for ICCP simulation have been implemented based on a specified: 1) fixed current for all anodes, 2) fixed potential for all reference cells, 3) potential range for all reference cells. The BEM has been shown to converge with an increasing number of reflections to an analytical expression. Lastly, the model was validated by comparing experimental results using a ship scale model to BEM simulations featuring: 1) Uniform material currents as boundary conditions, resulting in a low rRMS difference of 6.4%. 2) In situ measured polarization curves as boundary conditions, resulting in a rRMS difference of 7.6%.

CRediT authorship contribution statement

Stefan de Gijsel: Writing – review & editing, Writing – original draft, Visualization, Validation, Software, Methodology, Investigation, Formal analysis, Data curation, Conceptualization; **Nick J. Schilder:** Writing – review & editing, Writing – original draft, Visualization, Validation, Software, Methodology, Investigation, Formal analysis, Conceptualization; **Frits Kernkamp:** Writing – review & editing, Writing – original draft, Visualization, Validation, Resources, Methodology, Investigation, Conceptualization; **Bart Jan Peet:** Writing – review & editing, Writing – original draft, Supervision, Methodology, Investigation, Funding acquisition, Conceptualization; **Eugene Lepelaars:** Writing – review & editing, Supervision, Methodology, Investigation, Funding acquisition, Formal analysis, Conceptualization.

Data availability

The data that was used for the research described in the article is confidential.

Declaration of competing interest

The authors declare that they have no known competing financial interests or personal relationships that could have appeared to influence the work reported in this paper.

Acknowledgement

This work was funded by the Materiel and IT Command (Commit). Our thanks go to CORROSION for supplying a scaled down ICCP system, basin and expertise. We also thank the TNO Electrical Mechanical Department for PSM design and manufacturing.

Appendix A. Analytical solutions for linear elements

The integrals in (6) can be evaluated analytically. Analytical evaluation can be faster than computation using quadrature rules. For the expressions, several variables are defined:

$$\mathbf{R}_i = \mathbf{r}_i - \mathbf{r}, R_i = |\mathbf{R_i}|, \qquad i = 1, 2, 3, \tag{A.1}$$

$$\boldsymbol{\tau}_1 = \frac{\mathbf{r}_2 - \mathbf{r}_1}{|\mathbf{r}_2 - \mathbf{r}_1|}, \boldsymbol{\tau}_2 = \frac{\mathbf{r}_3 - \mathbf{r}_2}{|\mathbf{r}_3 - \mathbf{r}_2|}, \boldsymbol{\tau}_3 = \frac{\mathbf{r}_1 - \mathbf{r}_3}{|\mathbf{r}_1 - \mathbf{r}_3|}, \tag{A.2}$$

$$s_{ij} = \boldsymbol{\tau}_i \cdot \mathbf{r}_j, \qquad i, j = 1, 2, 3, \tag{A.3}$$

$$R_{01}^2 = R_3^2 - s_{13}^2, R_{02}^2 = R_1^2 - s_{21}^2, R_{03}^2 = R_2^2 - s_{32}^2, \tag{A.4}$$

$$\mathbf{c} = \frac{\mathbf{r}_1 + \mathbf{r}_2 + \mathbf{r}_3}{3}, \tag{A.5}$$

$$\mathbf{n}_0 = \frac{(\mathbf{r}_2 - \mathbf{r}_1) \times (\mathbf{r}_3 - \mathbf{r}_2)}{|(\mathbf{r}_2 - \mathbf{r}_1) \times (\mathbf{r}_3 - \mathbf{r}_2)|}, \tag{A.6}$$

$$\alpha = \mathbf{r}_1 \cdot (\mathbf{r}_2 \times \mathbf{r}_3), \tag{A.7}$$

$$\beta = R_1 R_2 R_3 + R_1(\mathbf{r}_2 \cdot \mathbf{r}_3) + R_2(\mathbf{r}_3 \cdot \mathbf{r}_1) + R_3(\mathbf{r}_1 \cdot \mathbf{r}_2), \tag{A.8}$$

$$\Omega = 2|\mathrm{atan2}(\alpha, \beta)|. \tag{A.9}$$

Furthermore, the following integral is evaluated (Okon and Harrington, 1982a):

$$I_1(\mathbf{r}, \mathbf{r}_1, \mathbf{r}_2, \mathbf{r}_3) = \iint_A \frac{1}{|\mathbf{r} - \mathbf{r}_0|} \mathrm{d}^2 r = (\mathbf{n}_1 \cdot \mathbf{r}_2) \ln\left(\frac{s_{13} + R_3}{s_{12} + R_2}\right) + (\mathbf{n}_2 \cdot \mathbf{r}_3) \ln\left(\frac{s_{21} + R_1}{s_{23} + R_3}\right) + (\mathbf{n}_3 \cdot \mathbf{r}_1) \ln\left(\frac{s_{32} + R_2}{s_{31} + R_1}\right) - |(\mathbf{r} - \mathbf{c}) \cdot \mathbf{n}_0| \Omega. \tag{A.10}$$

The first integral evaluates to

$$\begin{aligned} &\iint_A b_1(\mathbf{r}) \frac{\partial}{\partial n}\left(\frac{1}{|\mathbf{r} - \mathbf{r}_0|}\right) \mathrm{d}^2 r = \\ &- \frac{\mathbf{n}_3}{s_{32} - s_{31}}\left[s_{32} \ln\left(\frac{s_{32} + R_2}{s_{31} + R_1}\right) - R_2 + R_1\right] \\ &- \frac{\mathbf{n}_2}{s_{23} - s_{21}}\left[s_{23} \ln\left(\frac{s_{21} + R_1}{s_{23} + R_3}\right) - R_1 + R_3\right] \\ &+ \frac{\mathbf{n}_1 I_1(\mathbf{r}, \mathbf{r}_1, \mathbf{r}_2, \mathbf{r}_3)}{(\mathbf{r}_1 - \mathbf{r}_2) \cdot \mathbf{n}_1} \\ &+ \mathbf{n}_0 \left\{ \frac{\mathbf{n}_0 \cdot (\mathbf{r} - \mathbf{c})}{\mathbf{n}_1 \cdot (\mathbf{r}_1 - \mathbf{r}_2)} \left[\ln\left(\frac{s_{13} + R_3}{s_{12} + R_2}\right) + (\mathbf{n}_1 \cdot \mathbf{n}_2) \ln\left(\frac{s_{21} + R_1}{s_{23} + R_3}\right) + (\mathbf{n}_1 \cdot \mathbf{n}_3) \ln\left(\frac{s_{32} + R_2}{s_{31} + R_1}\right)\right] \right. \\ &\left. - \Omega b_1(\mathbf{r}) \mathrm{sign}\left[\mathbf{n}_0 \cdot (\mathbf{r} - \mathbf{c})\right] \right\}. \end{aligned} \tag{A.11}$$

The second integral, of which the analytical expression was first derived in Okon and Harrington (1982b), evaluates to

$$\begin{aligned} &\iint_A b_1(\mathbf{r}) \frac{1}{|\mathbf{r} - \mathbf{r}_0|} \mathrm{d}^2 r = \\ &b_1(\mathbf{r}) I_1(\mathbf{r}, \mathbf{r}_1, \mathbf{r}_2, \mathbf{r}_3) + \frac{1}{2(\mathbf{r}_1 - \mathbf{r}_2) \cdot \mathbf{n}_1} \\ &\cdot \left\{ (\mathbf{n}_1 \cdot \mathbf{n}_3)\left[s_{32} R_2 - s_{31} R_1 + R_{03}^2 \ln\left(\frac{s_{32} + R_2}{s_{31} + R_1}\right)\right] \right. \\ &+ \left[s_{13} R_3 - s_{12} R_2 + R_{01}^2 \ln\left(\frac{s_{13} + R_3}{s_{12} + R_2}\right)\right] \\ &\left. + (\mathbf{n}_1 \cdot \mathbf{n}_2)\left[s_{21} R_1 - s_{23} R_3 + R_{02}^2 \ln\left(\frac{s_{21} + R_1}{s_{23} + R_3}\right)\right] \right\}. \end{aligned} \tag{A.12}$$

References

Andjelić, Z., Smajić, J., Conry, M., 2007. BEM-Based Simulations in Engineering Design. Springer Berlin Heidelberg, Berlin, Heidelberg. pp. 281–352. https://doi.org/10.1007/978-3-540-47533-0_11.

Aoki, S., Kishimoto, K., 1991. Prediction of galvanic corrosion rates by the boundary element method. Mathem. Comput. Model. 15 (3-5), 11–22. https://doi.org/10.1016/0895-7177(91)90049-D.

Aoki, S., Kishimoto, K., Miyasaka, M., 1988. Analysis of potential and current density distributions using a boundary element method. Corrosion 44 (12), 926–932. https://doi.org/10.5006/1.3584967.

Chung, H.-J., Yang, C.-S., Jeung, G.-W., Jeon, J.-J., Kim, D.-H., 2011. Accurate prediction of unknown corrosion currents distributed on the hull of a naval ship utilizing material sensitivity analysis. IEEE Transac. Magnet. 47 (5), 1282–1285. https://doi.org/10.1109/CEFC.2010.5481301.

DeGiorgi, V.G., Thomas, E.D., Lucas, K.E., 1998. Scale effects and verification of modeling of ship cathodic protection systems. Eng. Anal. Bound. Elem. 22 (1), 41–49. https://doi.org/10.1016/S0955-7997(98)80012-X.

Ding-feng, Y., Pan, G., Zheng-xi, X., Tao, C., 2016. Analysis on ship's underwater static electric field with physical scale model. In: 2016 11th International Symposium on Antennas, Propagation and EM Theory (ISAPE), pp. 846–849. https://doi.org/10.1109/ISAPE.2016.7834092.

Ditchfield, R.W., McGrath, J.N., Tighe-Ford, D.J., 1995. Theoretical validation of the physical scale modelling of the electrical potential characteristics of marine impressed current cathodic protection. J. Appl. Electrochem. 25 (1), 54–60. https://doi.org/10.1007/BF00251265.

Donati, R., Le Cadre, J.-P., 2002. Detection of oceanic electric fields based on the generalised likelihood ratio test (GLRT). IEE Proc.-Radar, Sonar Navig. 149 (5), 221–230. https://doi.org/10.1049/ip-rsn:20020491.

Greengard, L., Rokhlin, V., 1997. A new version of the fast multipole method for the laplace equation in three dimensions. Acta Numer. 6, 229-269. https://doi.org/10.1017/S0962492900002725.

Guibert, A., Chadebec, O., Coulomb, J.-L., Rannou, C., 2009. Ships hull corrosion diagnosis from close measurements of electric potential in the water. IEEE Transac. Magnet. 45 (3), 1828–1831. https://doi.org/10.1109/TMAG.2009.2012796.

Guibert, A., Coulomb, J.-L., Chadebec, O., Rannou, C., 2010. Corrosion diagnosis of a ship mock-up from near electric-field measurements. IEEE Transac. Magnet. 46 (8), 3205–3208. https://doi.org/10.1109/TMAG.2010.2048098.

Hack, H.P., Janeczko, R.M., 1993. Verification of the Boundary Element Modelling Technique for Cathodic Protection of Large Ship Structures. Technical Report. Naval Surface Warefare Center Carderock Div Bethesda MD.

Huan, Y., Liu, Z., Shi, M., Jiang, Z., Xu, C., Li, S., 2023. Test and verification of electric field characteristics in seawater based on ship scaled model. In: 2023 IEEE 3rd International Conference on Power, Electronics and Computer Applications (ICPECA), pp. 326–329. https://doi.org/10.1109/ICPECA56706.2023.10076244.

Kalovelonis, D.T., Rodopoulos, D.C., Gortsas, T.V., Polyzos, D., Tsinopoulos, S.V., 2020. Cathodic protection of a container ship using a detailed BEM model. J. Marine Sci. Eng. 8 (5), 359. https://doi.org/10.3390/jmse8050359.

Keddie, A.J., Pocock, M.D., DeGiorgi, V.G., 2007. Fast solution techniques for corrosion and signatures modelling. WIT Transac. Eng. Sci. 54, 225–234. https://doi.org/10.2495/ecor070221.

Kim, Y.-S., Lee, S.K., Chung, H.-J., Kim, J.-G., 2018. Influence of a simulated deep sea condition on the cathodic protection and electric field of an underwater vehicle. Ocean Eng. 148, 223–233. https://doi.org/10.1016/j.oceaneng.2017.11.027.

Kythe, P.K., 1995. An introduction to boundary element methods. CRC Press. chapter 5.5. 1st edition.

Nale, M., Chadebec, O., Guichon, J.-M., Pinaud, O., Ramdane, B., Roche, V., Minola, M., Göeau, C., Bannwarth, B., 2023. Transient modelling of corrosion protection systems with BEM-electrical circuit hybrid model. IEEE Transac. Magnet. https://doi.org/10.1109/TMAG.2023.3255979.

Okon, E.E., Harrington, R.F., 1982a. The potential due to a uniform source distribution over a triangular domain. Int. J. Numer. Method. Eng. 18, 1401–1419. https://doi.org/10.1002/nme.1620180911.

Okon, E.E., Harrington, R.F., 1982b. The potential integral for a linear distribution over a triangular domain. Int. J. Numer. Method. Eng. 18, 1821–1828. https://doi.org/10.1002/nme.1620181206.

Ostrowski, J., Andjelic, Z., Bebendorf, M., Cranganu-Cretu, B., Smajic, J., 2006. Fast BEM-solution of laplace problems with H-matrices and ACA. IEEE Transac. Magnet. 42 (4), 627–630. https://doi.org/10.1109/TMAG.2006.871642.

Patterson, C., Sheikh, M.A., 1981. Discontinuous boundary elements for heat conduction. In: Numerical Methods in Thermal Problems. Vol. 2, pp. 25–34.

Peratta, A.B., Baynham, J.M.W., Adey, R.A., 2017. Computational modelling of cathodic protection systems for pipelines in multi-layer soil. WIT Transac. State Art Sci. Eng. 99, 245–257. https://doi.org/10.2495/978-1-78466-249-3/021.

Pratt, C.K., Young, J.C., Adams, R.J., Gedney, S.D., 2022. Boundary integral equation method for electrostatic field prediction in piecewise-homogeneous electrolytes. IEEE J. Mult. Multiphys. Comput. Techn. 8, 22–30. https://doi.org/10.1109/JMMCT.2022.3230664.

Riemer, D.P., Orazem, M.E., 2005. Modeling coating flaws with non-linear polarization curves for long pipelines. Corros. Cathod. Prot. Modell. Simul. 12, 225–259. https://doi.org/10.2495/1-85312-889-9/09.

Smajic, J., Andjelic, Z., Bebendorf, M., 2007. Fast BEM for eddy-current problems using H-matrices and adaptive cross approximation. IEEE Transac. Magnet. 43 (4), 1269–1272. https://doi.org/10.1109/TMAG.2006.890971.

Smajic, J., Cranganu-Cretu, B., Ostrowski, J., Andjelic, Z., 2006. Stationary voltage and current excited complex system of multimaterial conductors with BEM. IEEE Transac. Magnet. 42 (4), 707–710. https://doi.org/10.1109/TMAG.2006.871601.

Sun, W., 2002. Relaxation iterative algorithms for solving cathodic protection systems with non-linear polarization curves. Int. J. Numer. Method. Eng. 55 (4), 401–412. https://doi.org/10.1002/nme.504.

Telles, J.C.F., Mansur, W.J., Wrobel, L.C., 1984. On boundary elements for external potential problems. Mech. Res. Commun. 11 (6), 373–377. https://doi.org/10.1016/0093-6413(84)90044-2.

Wang, B., Feng, Y., Zhou, X., Pieraccini, S., Scialò, S., Fidelibus, C., 2022. Discontinuous boundary elements for steady-state fluid flow problems in discrete fracture networks. Adv. Water Resour. 161, 104125. https://doi.org/10.1016/j.advwatres.2022.104125.

Wang, Y., KarisAllen, K.J., 2010. Comparison of impressed current cathodic protection numerical modeling results with physical scale modeling data. Corrosion 66 (10), 105001–1–105001–15. https://doi.org/10.5006/1.3500829.

Wrobel, L.C., Miltiadou, P., 2004. Genetic algorithms for inverse cathodic protection problems. Eng. Anal. Bound. Elem. 28 (3), 267–277. https://doi.org/10.1016/S0955-7997(03)00057-2.